Atmos. Meas. Tech., 5, 181–192, 2012
www.atmos-meas-tech.net/5/181/2012/
doi:10.5194/amt-5-181-2012

Atmospheric Measurement Techniques

Quantification of gas-phase glyoxal and methylglyoxal via the Laser-Induced Phosphorescence of (methyl)GLyOxal Spectrometry (LIPGLOS) Method

S. B. Henry[1], **A. Kammrath**[1,*], **and F. N. Keutsch**[1]

[1]Department of Chemistry, University of Wisconsin-Madison, 1101 University Avenue, Madison, WI 53706, USA
[*]now at: Kimberly-Clark Corporation, 2100 Winchester Road, Neenah, WI 54956, USA

Correspondence to: F. N. Keutsch (keutsch@chem.wisc.edu)

Received: 20 September 2011 – Published in Atmos. Meas. Tech. Discuss.: 5 October 2011
Revised: 12 January 2012 – Accepted: 13 January 2012 – Published: 23 January 2012

Abstract. Glyoxal and methylglyoxal are key products of oxidative photochemistry in the lower troposphere. Reliable measurements of such compounds are critical for testing our understanding of volatile organic compound (VOC) processing in this region. We present a new method for obtaining sensitive, high time resolution, in situ measurements of these compounds via laser-induced phosphorescent decays. By exploiting the unique phosphorescent lifetimes for each molecule, this method achieves speciation and high-sensitivity quantification of both molecules. With two different light sources at different wavelengths, the lowest 3σ limits of detection observed during calibration with this method are 11 pptv in 5 min for glyoxal and 243 pptv in 5 min for methylglyoxal. During ambient measurements of glyoxal, a 3σ limit of detection of < 4.4 pptv in 5 min was observed. Additionally, this method enables the simultaneous measurement of both glyoxal and methylglyoxal using a single, non-wavelength-tunable light source, which will allow for the development of inexpensive ($\sim$\$40 k) and turnkey instrumentation. The simplicity and affordability of this new instrumentation would enable the construction of a long-term, spatially distributed database of these two key species. This chemical map can be used to constrain or drive regional or global models as well as provide verification of satellite observations.

1 Introduction

Glyoxal and methylglyoxal are nearly ubiquitous and are generated through volatile organic compound (VOC) oxidation by the HO_x/NO_x cycle ($HO_x = HO_2 + OH$, $NO_x = NO_2 + NO$), a photochemically driven oxidation process. This process, which oxidizes volatile organic compounds (VOCs) that are emitted by both anthropogenic and biogenic sources, has the potential to generate secondary organic aerosol (SOA) precursors and tropospheric ozone (O_3). Both SOA and O_3 have been shown to have detrimental effects on human health and climate (Lippmann, 1991; Stieb et al., 2000; Lohmann, 2005; Isaksen et al., 2009). In an effort to understand these processes, observations of the VOC oxidation products, as well as the VOCs themselves, provide an important constraint for validating chemical models of the atmosphere by both driving these models as well as being a point of comparison and identifying inaccuracies within the model mechanism. Glyoxal and methylglyoxal have been shown to partition in appreciable amounts to SOA despite their low molecular weight by reacting to form lower volatility products, such as oligomers or organosulfates, inside the aerosol (Hallquist et al., 2009; Yu et al., 2011). Glyoxal was reported to account for up to 15 % of the mass of SOA in Mexico City (Volkamer et al., 2007).

Glyoxal and methylglyoxal have short lifetimes of a few hours during the day, primarily due to photolysis and reaction with OH (Volkamer et al., 2005a; Fu et al., 2008).

Thus, both are tracers of local or regional chemistry since they exist on shorter timescales than large scale transport. They occur in detectable quantities over much of the planet since they are produced from both anthropogenic and biogenic emissions. Low tens to low hundreds of pptv for both glyoxal (15–190 pptv) and methylglyoxal (<50–320 pptv) have been reported in rural, urban, and marine regions in this work (Sect. 4) and others (Lee et al., 1995; Munger et al., 1995; Spaulding et al., 2003; Fu et al., 2008; Huisman et al., 2008; Vrekoussis et al., 2009; Sinreich et al., 2010). However, glyoxal concentrations in Mexico City have been recorded as high as 1.82 ppbv (Volkamer et al., 2005a). Globally, the majority of glyoxal (47 %) and methylglyoxal (79 %) comes from isoprene (Fu et al., 2008). Isoprene makes up a large portion (1/3 to 1/2) of globally emitted carbon at an estimated rate of 503 Tg yr^{-1} (Guenther et al., 1995). Glyoxal and methylglyoxal have direct yields from isoprene of 2.1 % (Galloway et al., 2011) and 4.2 % (Galloway et al., 2011; Paulot et al., 2009), respectively. The remainder of glyoxal comes from acetylene (Fu et al., 2008) and various alkenes (e.g. 2-methyl-3-buten-2-ol, propene, or 2-butene (Chan et al., 2009; Volkamer et al., 2007)) and aromatics (e.g. benzene, toluene, and p-xylene (Volkamer et al., 2005b, 2007)). The methylglyoxal that does not come from isoprene is yielded by acetone (Fu et al., 2008), alkenes (e.g. methylvinylketone or 2-Methylprop-2-enal (Galloway et al., 2011)), and aromatics (e.g. toluene, (m/p)-xylene (Tuazon et al., 1984)).

Several techniques already exist for detection of these important dicarbonyls. SCanning Imaging Absorption SpectroMeter for Atmospheric CartograpHY (SCIAMACHY), Global Ozone Monitoring Experiment (GOME) and GOME-2 on satellites are used to retrieve global glyoxal datasets (Wittrock et al., 2006; Vrekoussis et al., 2009, 2010); however, validation of these satellites retrievals with ground-based measurement is required for data quality purposes. The Madison Laser-Induced Phosphorescence (Mad-LIP) instrument can acquire high sensitivity (3σ limit of detection (LoD) of 18 pptv per one min), high time resolution (up to 3 Hz), in situ single point measurements of glyoxal (Huisman et al., 2008). Cavity Enhanced Differential Optical Absorption Spectroscopy (CEDOAS) is also capable of sensitive, fast, in situ single point measurements of both glyoxal (3σ LoD as low as 28.5 pptv per one min) and methylglyoxal (3σ LoD as low as 170 pptv per one minute) (Thalman and Volkamer, 2010). A similar spectroscopic method, incoherent broadband cavity enhanced absorption spectroscopy (IBBCEAS), can achieve a 3σ LoD for glyoxal of 87 pptv per one min (Washenfelder et al., 2008). Derivatization using DNPH-coated filters followed by HPLC analysis is a comparatively simple and inexpensive method of detection for both glyoxal (1.5 ppbv per four hours) and methylglyoxal (1.3 ppbv per four hours), but suffers from high detection limits, poor temporal resolution and potentially significant interferences (US EPA, Center for Environmental Research Information, Reasearch and Development, 1999; Ho and Yu, 2004).

In this study, we present the Laser-Induced Phosphorescence of (methyl)GLyOxal Spectrometry (LIPGLOS) method, a novel and sensitive approach for measuring glyoxal and methylglyoxal that exploits the characteristic distribution of their phosphorescent photons with respect to time. We begin by describing the instrumental setup as well as data collection. We then discuss how the raw data is analyzed to retrieve glyoxal and methylglyoxal signals. The sensitivity is then characterized with a series of calibrations. To validate the concentrations observed by this method, simultaneous glyoxal calibrations of the Mad-LIP instrument using its native gated photon integration method and the LIPGLOS method was performed. Finally, an intercomparison of glyoxal data between the two methods during ambient sampling is examined.

2 Methods

2.1 Measurement principle

The relaxation of a population of excited molecules by any given pathway can be described by:

$$\frac{d[X^*]}{dt} = \frac{-1}{\tau}[X^*] \quad (1)$$

The excited analyte is represented by $[X^*]$. The lifetime of the excited state, τ, is unique to a specific species undergoing a particular relaxation pathway under a given set of conditions such as temperature, pressure, and in the case of luminescence, quantity of quenching molecules present. The solution to Eq. (1) is an exponential decay, with a decay constant of $1/\tau$ and a prefactor of $[X^*]_o$ (initial value of $[X^*]$). During relaxation by luminescence, the intensity of the light emitted is directly proportional to $[X^*]$. Therefore, when a population of phosphorescing molecules is observed, the light will have the same temporal distribution as the excited state population; in this case, an exponential decay. If there is more than one phosphorescing species present, each with their own unique lifetime, the temporal distribution of photons is simply the sum of their exponential decays.

The fundamental difference between the LIPGLOS and gated photon integration that is used by the Mad-LIP instrument is how the photon-counting signal is used to derive concentrations. In the latter technique, signals are determined by integrating the phosphorescence signal over the entire decay interval (typically on the order of 10 s of µs). As described in more detail below, differentiation of glyoxal and background signals via this technique requires dithering the wavelength of a tunable laser. In contrast, the LIPGLOS method utilizes the time-dependent decay of the phosphorescence signal to distinguish between these two molecules, allowing for speciation of both compounds at a single wavelength.

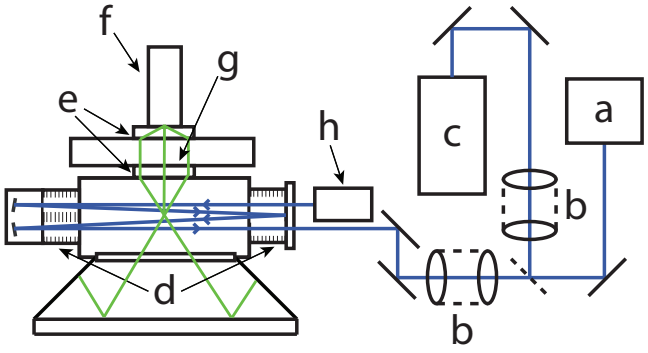

Fig. 1. Schematic drawing of the experimental setup. The components are: light source **(a)**, focusing optics **(b)**, cavity ringdown cell **(c)**, light baffles **(d)**, collimating optics **(e)**, single photon counter photomultiplier tube **(f)**, optical bandpass filter **(g)**, laser power meter **(h)**. Components **(d–g)** are inside the white type multipass cell. A pump (not shown) draws air through the detection cell at ∼20 SLM.

2.2 Experimental setup

The experimental setup (Fig. 1) was similar to that of the Mad-LIP instrument, which is described in detail elsewhere (Huisman et al., 2008). The primary differences were the light source as well as additional data collection protocols and hardware as detailed below. Included here is a brief description of the setup, which consists of the main components: light source, detection cell, data acquisition card, and cavity ringdown cell.

2.2.1 Light source

The use of two different light sources was investigated independent of one another as this method only requires a single light source. Using these two different light sources allows a comparison between two different kinds of light sources, one a research-grade pulsed Ti:Sapphire laser (∼$125 k) and the other a simpler and less expensive continuous wave diode laser (∼$10 k).

The diode laser is a fixed-wavelength CW light source (DL445-050-O, CrystaLaser) which emits 50 mW of 444.457 nm (λ_{CL}) light with a nominal spectral bandwidth of 1 nm (FWHM) and a TEM_{00} beam mode. An optional functionality was added by the manufacturer to allow turning the laser on and off by TTL logic. The laser transition time between the on and off states is <10 ns, effectively instantaneous for its application in these experiments. During operation, this laser was held on for 32 µs, and turned off for the same duration which resulted in a repetition rate of 15 625 Hz.

The other light source was a custom tunable Ti:Sapphire laser (TU series, Photonics Industries International, Inc.), which was used to generate 440.136 nm ($\lambda_{T:S,H}$) and 440.104 nm ($\lambda_{T:S,L}$) light. The former was chosen because it is centered on a large, sharp (∼.06 nm wide) rovibrational absorption feature of glyoxal, and the latter is a nearby position that is off of the feature with an optical cross-section ∼3 times lower. The optical cross-section of methylglyoxal is nearly identical (<0.2 % different) at either $\lambda_{T:S,H}$ and $\lambda_{T:S,L}$ which is ∼10.2 and ∼3.5 times smaller than the respective glyoxal optical cross-sections (Meller et al., 1991; Volkamer et al., 2005c). A summary of these cross-sections can be found in Table 1. The laser operated at 3 kHz, an average power of 60 mW, and a bandwidth of <0.00078 nm.

Three different wavelengths are considered in this study to investigate how the measurement sensitivities change with optical cross-sections that vary with wavelength. In addition, the interference between glyoxal and methylglyoxal can be probed by changing their relative sensitivities (see Sect. 3.2). Finally, comparing the CrystaLaser as an alternative to the much more expensive Ti:Sapphire laser requires data taken at λ_{CL}.

2.2.2 Detection cell

The excitation light was aligned into a White-type multipass cell which allows for a longer absorption path length, thereby improving instrument sensitivity. The average light power directed into the cell was typically ∼40 % of power emitted from the laser. For both lasers, this reduction in power was due to scatter/absorption by optics and two beam splitters: one to direct power to the cavity ringdown cell (Sect. 2.2.4) and another to a wavelength meter. An additional power loss unique to the CrystaLaser is incurred since it is operated with a duty cycle of 50 %, resulting in a factor of 2 power loss from its CW rated 50 mW. During operation, 32 passes are used in the detection volume of the cell (∼1/2 L) that ambient air is drawn through. Phosphorescence photons were collected and collimated with a lens (biconvex, diameter 38.1 mm, ROC_1 = 100 mm, ROC_2 = 30.9 mm, CVI Laser), then passed through an optical 520 ± 20 nm bandpass filter (Barr Associates), and finally focused with a second, identical lens onto the entire active area of the detector, a single photon-counting photomultiplier tube (PMT) (H7421-40, Hamamatsu). The output of this PMT was a TTL pulse, 30 ns wide. A light trap, placed opposite the detector, ensures a low background signal.

The volume between the optic elements and the detection volume, as well as the light trap, were continuously flushed with zero air (total flow 500 SCCM), which protects against fouling of the optics during prolonged operation and eliminates dead volumes within the cell which may bias measurement. The purge flow is typically small (<2.5 %) relative to the bulk sample flow, nominally 20 standard liters per minute (SLM). PTFE tubing and valves were used in the system whenever possible as they do not exhibit significant glyoxal uptake at ambient concentrations (Huisman et al., 2008). To minimize influence from ambient light and ensure

Table 1. Summary of the wavelengths and the corresponding optical cross-section for their respective molecules.

Species	λ (symbol)	λ/FWHM (nm)	$^{\dagger}\sigma$ (cm^2 $molecule^{-1}$)
Glyoxal	T:S,H	$440.136/7.8\times10^{-4}$	10.20×10^{-19}
	T:S,L	$440.104/7.8\times10^{-4}$	3.42×10^{-19}
	CL	444.457/1	1.05×10^{-19}
Methyl-glyoxal	T:S,H	$440.136/7.8\times10^{-4}$	1.00×10^{-19}
	T:S,L	$440.104/7.8\times10^{-4}$	1.00×10^{-19}
	CL	444.457/1	0.96×10^{-19}

†Glyoxal and methylglyoxal cross-sections measured by Volkamer et al. (2005c) and Meller et al. (1991), respectively.

a low background signal, the inside of the cell was coated with a mixture of carbon black (Sigma-Aldrich) and black paint (MH-2200, Alion Science and Technology). The entire cell was heated to ∼35 °C with a series of flexible, resistive Kapton heaters controlled through feedback from corresponding thermistors. This heating minimizes deposition of analytes on the cell walls and stabilizes alignment. The cell was maintained at 100 Torr, which was empirically determined to yield the optimum signal by balancing increasing number density (molecules cm^{-3}) with de-excitation by quenching with oxygen.

2.2.3 Data acquisition card

The single photon counting PMT emits a single 30 ns TTL pulse every time a photon is detected. This output is fed into the data acquisition card which records it as an analog signal of voltage versus time after the falling edge of the laser control signal. The arrival times of the pulses are then extracted from this waveform by finding at what times after the laser pulse the analog data exceeds a specified threshold value for a specified amount of time. Once the period of integration is complete, a histogram of these arrival times is then created (Fig. 2) and saved on the hard disk for later analysis. Additional instrumental diagnostics, such as temperature and pressure within the cell, were also recorded. Even though a single data acquisition (DAQ) card is required to digitize the signal from the PMT, two different cards had to be used in different situations independent of one another due to equipment availability.

A high-speed digitizer card from Alazar Technologies Inc. (ATS9462-002-USD) has a high time resolution (5.55 ns) and fast data acquisition abilities that allow data to be recorded after each laser shot, even at the CrystaLaser repetition rate of 15 625 Hz. A unity duty cycle was accomplished by the usage of an on-board memory buffer, allowing simultaneous data acquisition and communication of waveforms. The entire data buffer, consisting of low hundreds of laser shots of data, was analyzed simultaneously.

The other DAQ card from GaGe was used only for ambient data acquisition. This possessed a coarser, yet still adequate, time resolution (10 ns) with a duty cycle of ∼48 % at 3 kHz. The lower duty cycle resulted from the data collection and transfer occurring on the card in series. To be comparable to the faster digitizer card from Alazar Technologies Inc., the integration time for the GaGe card is reported assuming it had a duty cycle of 100 % (e.g. 120 s of actual integration time will be reported as 57.6 s of comparable integration time).

2.2.4 Cavity Ringdown Spectroscopy

Instrumental calibrations were performed using Cavity Ringdown Spectroscopy (CRDS), an absolute quantification method in that it relies only on well-documented absorption cross-sections. Further details about the theory of this method is described elsewhere (O'Keefe and Deacon, 1988).

A cavity 62 cm long and 0.635 cm in diameter was formed between two parallel, highly reflective mirrors with a radius of curvature of 1 m (99.995 % reflectance) (901-0010-0440, Los Gatos Research Inc.). The bulk of the cavity was encased in a 3/8″ O.D., 1/4″ I.D. PTFE tube. Halfway along the cavity, a PTFE tee was used as an inlet for calibrant gas. On each end of the cavity, the mirror mounts were coupled via metal bellows to a Teflon PTFE tee which coupled the cell to exhausts ports for the cell. The dead volumes between the exhaust ports and the mirrors were flushed with zero air (Airgas, Inc.) through a 200 standard cubic centimeter per minute (SCCM) flow controller (1779A, MKS Instruments) to prevent optics fouling as well as bias. This purging did not allow any sample gas to mix beyond the exhaust ports, fixing the physical absorber path length to 42 cm. This cell design is based on to the NOAA NO_3 ringdown cell design (Dubé et al., 2006; Osthoff et al., 2006). The entire cavity length between, and including, the exhaust tee fittings was enclosed in a 1.5″ by 1.5″ block of aluminum which was maintained at a constant temperature (∼35 °C) to discourage analyte deposition inside the cavity.

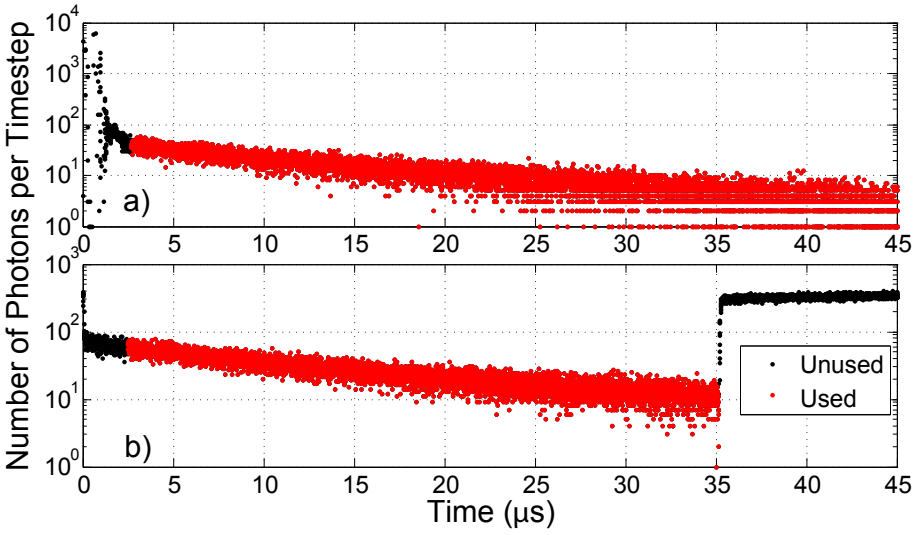

Fig. 2. Timestep in y-axis label corresponds to temporal resolution of Alazar data acquisition card (5.55 ns). **(a)** Example histogram corresponding to 1000 pptv glyoxal collected with Ti:Sapphire laser in 5 min. The initial large peak is the laser pulse. **(b)** Example histogram corresponding to 4200 pptv glyoxal collected with CrystaLaser in 15 min. Both the initial peak as well as the plateau after the used data results from laser scatter.

A 10 SCCM flow controller (1779A, MKS Instruments) supplied calibrant gas that was then diluted by zero air (Airgas, Inc.). The zero air was delivered by a 200 SCCM flow controller (1779A, MKS Instruments) at a rate which made up the remainder to a total flow of 100 SCCM of diluted calibrant. The purge was held at 100 SCCM using a 200 SCCM flow controller (1779A, MKS Instruments). To maintain a constant cell pressure and therefore achieve a stable baseline, both the purge and the diluted calibrant flows were held constant.

Laser pulses were introduced into the cavity through one of the high-reflectivity mirror. With each reflection, a small quantity of light escaped through the mirrors. On the opposite side of this cavity, a PMT (H5783, Hamamatsu), guarded by a 440 nm bandpass filter, detected this escaped light. Loss of photons within the cavity is a first-order process, thus the light leaking from the cavity has the characteristics of an exponential decay. The loss of light within the cavity, whether the light is absorbed by a chemical, transmitted through/absorbed by the mirrors, or scattered by gas/aerosols, can be quantified by the decay lifetime, τ. The number density of a chemical absorber (molecules cm^{-3}) can be determined by relating two determined lifetimes, those determined with and without the presence of the absorber, by the following equation:

$$N_{\mathrm{d}} = \frac{1-R}{\sigma \ell_{\mathrm{a}}}\left(\frac{\tau_{\mathrm{o}}-\tau}{\tau}\right) \quad (2)$$

where N_{d} is the number density of the absorber, R is mirror reflectivity, σ is the absorption cross-section, ℓ_{a} is the path length of the absorber, τ and τ_{o} are the lifetimes with and without the absorber, respectively (Zalicki and Zare, 1994).

2.2.5 Instrumental configurations

Experiments performed in this study utilized three different instrumental configurations with respect to light sources and data acquisition cards. The first configuration, the CrystaLaser with the Alazar DAQ card, was used for all data collected at λ_{CL}. The second configuration, the tunable Ti:Sapphire laser with the Alazar DAQ card, was used for all data collected at $\lambda_{\mathrm{T:S,H}}$ and $\lambda_{\mathrm{T:S,L}}$ except during the ambient intercomparison between LIPGLOS and gated photon integration. During these last experiments, a third configuration used the Ti:Sapphire laser with the GaGe DAQ card.

3 Data and signal characterization

3.1 Analysis

The collected histogram includes several sources of photons: laser scatter, fluorescence of cell walls and gas-phase species, and phosphorescence. To eliminate the laser scatter and fluorescence, which are both short-lived compared to phosphorescence, the fitting began 2.5 μs after the laser pulse and extended to either the end of the recorded data set, as in the case of the Ti:Sapphire (45 μs, Fig. 2a), or until the laser was turned back on, as with the CrystaLaser (35 μs, Fig. 2b). Due to this gated temporal selectivity, this method does not suffer from interference from unfiltered ambient air at 60 % relative humidity or NO_2 fluorescence (Huisman

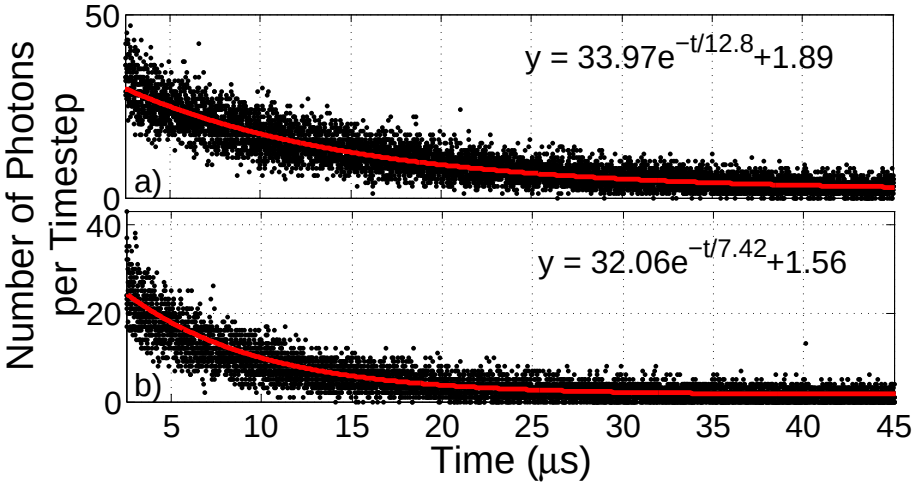

Fig. 3. Timestep in y-axis label corresponds to temporal resolution of Alazar data acquisition card (5.55 ns). Examples of decays for 5 min integration for glyoxal (**(a)**, 290 pptv) and methylglyoxal (**(b)**, 5400 pptv) taken with the Ti:Sapphire laser with lines of best fit to Eq. (3).

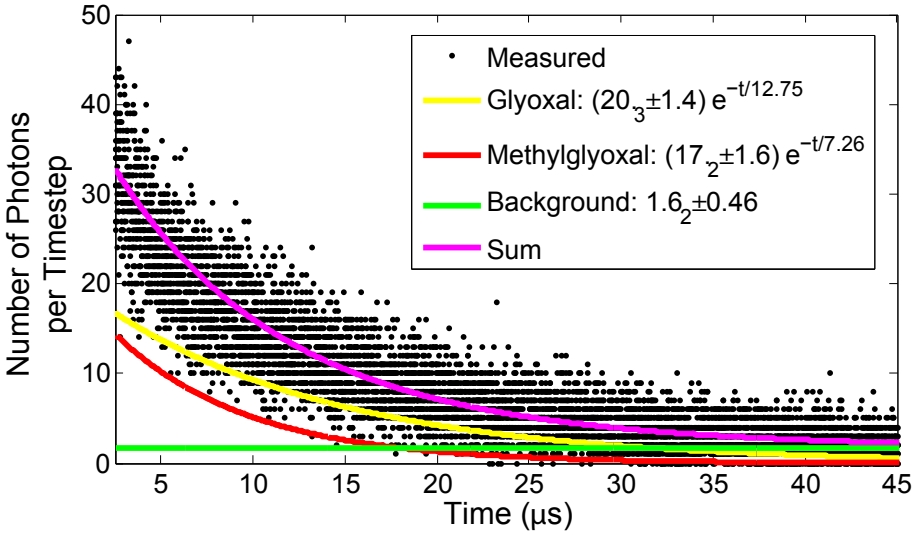

Fig. 4. Timestep in y-axis label corresponds to temporal resolution of Alazar data acquisition card (5.55 ns). Decay of 5 min integration for a mixture of glyoxal (180 pptv) and methylglyoxal (2500 pptv) taken with the Ti:Sapphire laser at $\lambda_{T:S,H}$ with line of best fit to Eq. (4) and its individual components.

et al., 2008). This, however, does not eliminate signal from dark counts or stray ambient light. These two contributions are manifested as time independent background.

Histograms collected from a mixture of glyoxal and methylglyoxal, such as in ambient air, are a linear combination of exponential decays with the respective characteristic lifetimes for glyoxal and methylglyoxal. These lifetimes were determined individually via a series of laboratory calibrations. The decays during these calibrations were fit using an iterative least squares algorithm to Eq. (3):

$$D(t) = Ae^{-t/\tau} + B \quad (3)$$

Where A is the prefactor, t is time, τ is the phosphorescent lifetime, and B is the background. Example decays from the glyoxal and methylglyoxal calibrations are shown in Fig. 3. The τ for glyoxal and methylglyoxal was determined in air at 100 Torr to be $12.75_3 \pm 0.08$ µs and $7.26_3 \pm 0.03$ µs, respectively. Once these lifetimes were established, the glyoxal and methylglyoxal contributions were extracted from decays collected. This was performed by fitting the decays to Eq. (4) using a least squares method:

$$D(t) = A_{gly}e^{-t/\tau_{gly}} + A_{mgly}e^{-t/\tau_{mgly}} + B \quad (4)$$

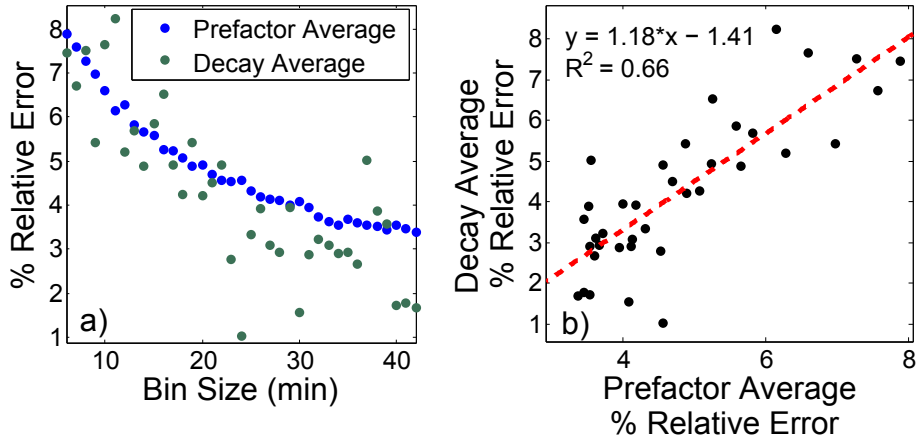

Fig. 5. Comparison between the two methods of averaging: prefactor averaging, where the decays of shortest integration are fit followed by averaging the prefactors to desired time resolution, and decay averaging, where the decay is averaged over desired period of integration followed by fitting. **(a)** The percent relative errors for the two averaging methods versus the averaging bin size. **(b)** The correlation between the relative errors in the two averaging methods with the accompanying trend line and equation.

where τ_x is the phosphorescent lifetime of the analyte which was determined in the previously mentioned experiments, A_x is the contribution of the analyte to the, and B is the background. An example of this fitting is presented in Fig. 4.

The nature of data collection and the analysis permits two distinct methods of averaging: fitting the decays followed by averaging the prefactors (prefactor averaging), or fitting to an averaged decay (decay averaging). To determine the performance of each method, a constant concentration was sampled for two hours at one minute integration. Figure 5a demonstrates how the relative error changes with averaging bin size for both methods. The near unity slope in the line of best fit in Fig. 5b between the relative errors of the two methods taken at the different bin sizes illustrates that they have the same behavior.

3.2 Calibration

Glyoxal and methylglyoxal calibrant gases were synthesized from glyoxal trimer dihydrate (G680-5, Sigma-Aldrich) and 40 wt. % aqueous pyruvaldehyde solution (w296902, Sigma-Aldrich) as described elsewhere (Kroll et al., 2005; Galloway et al., 2009). The gases were stored in separate 12 L glass bulbs at a concentration of ∼1 % with a balance gas of N_2. Approximately 2 cm^3 of this gas was transferred to a stainless steel cylinder with an inner surface prepared with a fluorinated polymer solution (PFC 802A, FluoroPel) to minimize wall loss. We have empirically determined that calibrant concentrations in these containers are stable for months.

After the standard gas was characterized via CRDS (see Sect. 2.2.4), independent phosphorescent calibrations were performed for glyoxal and methylglyoxal at concentrations between low pptv to low ppbv. Calibrant mixing ratios in the LIP detection cell were determined by diluting different calibrant gas flow rates that were controlled with a 10 SCCM flow controller (1779A, MKS Instruments) with ∼20 SLM zero air that was controlled by a 100 SLM flow controller (1559A, MKS Instruments).

Once the analyte concentration inside the cell was stabilized, a histogram was taken. The resulting decay was fit to Eq. (4) to retrieve the contribution of glyoxal and methylglyoxal. A calibration curve was generated from the known concentrations in the cell and their given responses as determined from the fit. Table 2 summarizes the resulting calibration curves from these experiments. The LoDs included in the table are three times the fit error of the blank in units of pptv.

The calibration factors for $\lambda_{T:S,H}$ and $\lambda_{T:S,L}$ scale with optical cross-section. An approximately threefold decrease in glyoxal's optical cross-section corresponds to a ∼3.75-fold decrease in sensitivity, whereas the methylglyoxal cross-section and sensitivity change very little. The sensitivities attained at λ_{CL} not only have different cross-sections, but they also were with a light source of different peak power, pulse width, and repetition rate. Because of these differences, a sensitivity comparison would be inappropriate.

Experiments were also performed to investigate the sensitivity of biacetyl due to its similar structure (CC(=O)C(=O)C) and optical cross-section to glyoxal and methylglyoxal ($\sigma_{biacetyl} = 6.87 \times 10^{-20}$ cm^2 $molecule^{-1}$ (Horowitz et al., 2001) is $0.65\sigma_{methylglyoxal}$ and $0.51\sigma_{glyoxal}$ at λ_{CL} which is where all three cross-sections are the most similar out of the three wavelengths used). The LIPGLOS method was determined to be insensitive to biacetyl under the typical conditions of operation. This is consistent with previous work which demonstrated that the phosphorescence of biacetyl is efficiently quenched with trace amounts of oxygen (Turro and Engel, 1969).

Table 2. Summary of the results from the six different calibrations with only either glyoxal or methylglyoxal present inside the detection cell. All data presented here is 5 min integration. Data taken at λ_{CL} has been scaled from 15 min integration to 5 min for purpose of comparison. For purposes of comparison, Mad-LIP has an extrapolated 3σ LoD of 1 pptv per 5 min.

Species	λ (symbol)	Sensitivity (prefactor ppt_v^{-1} mW^{-1})	Intercept (prefactor mW^{-1})	R^2	3σ LoD (pptv)
Glyoxal	T:S,H	$(1.5_0 \pm 0.1) \times 10^{-2}$	$-0.4_0 \pm 0.3$	0.991	11
	T:S,L	$(4.0_0 \pm 0.2) \times 10^{-3}$	$-0.4_5 \pm 0.1$	0.996	37
	CL	$(3.59_8 \pm 0.07) \times 10^{-4}$	$0.04_8 \pm 0.01$	0.999	146
Methyl-	T:S,H	$(6.30_8 \pm 0.07) \times 10^{-4}$	$1.79_4 \pm 0.02$	1.000	322
glyoxal	T:S,L	$(6.8_4 \pm 0.3) \times 10^{-4}$	$1.78_8 \pm 0.08$	0.996	269
	CL	$(1.5_4 \pm 0.1) \times 10^{-4}$	$0.04_2 \pm 0.02$	0.991	243

Table 3. Summary of the results from the six different calibrations with both glyoxal and methylglyoxal present inside the detection cell. The last column represents the relative percent difference in sensitivities as determined in a pure calibration versus in a mixture ($100 \times$ (Sensitivity$_{mixed}$ − Sensitivity$_{pure}$)/Sensitivity$_{pure}$). During experiments at $\lambda_{T:S,L}$, glyoxal ranged from 140 to 1000 pptv and methylglyoxal ranged from 130 to 5400 pptv. During experiments at $\lambda_{T:S,H}$, glyoxal ranged from 140 to 750 pptv and methylglyoxal ranged from 130 to 5400 pptv. During experiments at λ_{CL}, glyoxal varied from 720 to 4200 pptv while methylglyoxal varied 730 to 6800 pptv.

Species	λ	Sensitivity (prefactor ppt_v^{-1} mW^{-1})	Intercept (prefactor mW^{-1})	R^2	Sensitivity Difference (%)
Glyoxal	T:S,H	$(1.27_3 \pm 0.07) \times 10^{-2}$	$-0.1_8 \pm 0.2$	0.977	−15.1
	T:S,L	$(3.7_9 \pm 0.1) \times 10^{-3}$	$-0.43_5 \pm 0.07$	0.989	−5.3
	CL	$(2.8_9 \pm 0.4) \times 10^{-4}$	$-0.05_8 \pm 0.09$	0.905	−19.7
Methyl-	T:S,H	$(2._5 \pm 3) \times 10^{-4}$	$0.4_2 \pm 0.4$	0.064	−60.3
glyoxal	T:S,L	$(5._2 \pm 1) \times 10^{-4}$	$1.2_8 \pm 0.2$	0.539	−24.0
	CL	$(1.5_2 \pm 0.2) \times 10^{-4}$	$0.07_2 \pm 0.06$	0.944	−1.3

To investigate the robustness of the speciation method, various mixtures of glyoxal and methylglyoxal of different relative concentrations were sampled and analyzed (Table 3). This table does not have an LoD column because the LoD varies with the mixing ratio of the other component. This is because when a bi-exponential histogram is considered, the major component effectively serves as an increased background for the minor component, which results in an increased LoD for the minor signal. To best demonstrate this, $\lambda_{T:S,H}$ is used for the most dramatic difference in sensitivities between the two components. For example, the 3σ LoD for methylglyoxal doubles in the presence of 1 ppbv glyoxal when compared to the blank. Another example of this dependence is the decreased R^2 associated with $\lambda_{T:S,H}$ and $\lambda_{T:S,L}$ for methylglyoxal in the mixture calibration. Since the glyoxal signal is greater than the methylglyoxal signal it is more difficult to detect the methylglyoxal, this leads to a noisier methylglyoxal signal which results in a higher LoD and the lower correlation coefficients. Sensitivities from the other mixture calibrations do not deviate more than 20 % from those established in the pure calibrations.

To further confirm the independence of the sensitivities of glyoxal and methylglyoxal, experiments were conducted in which the concentration of methylglyoxal was varied to be 66 %, 143 %, and 363 % of a constant glyoxal concentration. The relative standard deviation of these three glyoxal signals determined at $\lambda_{T:S,H}$ and $\lambda_{T:S,H}$ was 6 % and 4 %, respectively. Another set of analogous experiments was performed at λ_{CL} where the methylglyoxal concentration was varied to be 123 %, 271 %, and 344 % of the constant glyoxal concentration. The variability in the resulting glyoxal measurements was 15 %. The fact that the calibration curves maintain a high correlation coefficient even in the presence of variable mixtures of glyoxal and methylglyoxal indicates that the two values can indeed be determined independent of one another.

A simultaneous calibration was performed using both pure and mixed concentrations to compare the LIPGLOS method to the established measurement of gated photon integration via the Mad-LIP instrument, using both $\lambda_{T:S,H}$ and $\lambda_{T:S,L}$. Since the Mad-LIP instrument is insensitive to methylglyoxal, only the glyoxal data was considered. Figure 6 demonstrates that the measurements were highly correlated with R^2 values of 0.98 and 0.97 and 1-to-1 within error 1.00 ± 0.04

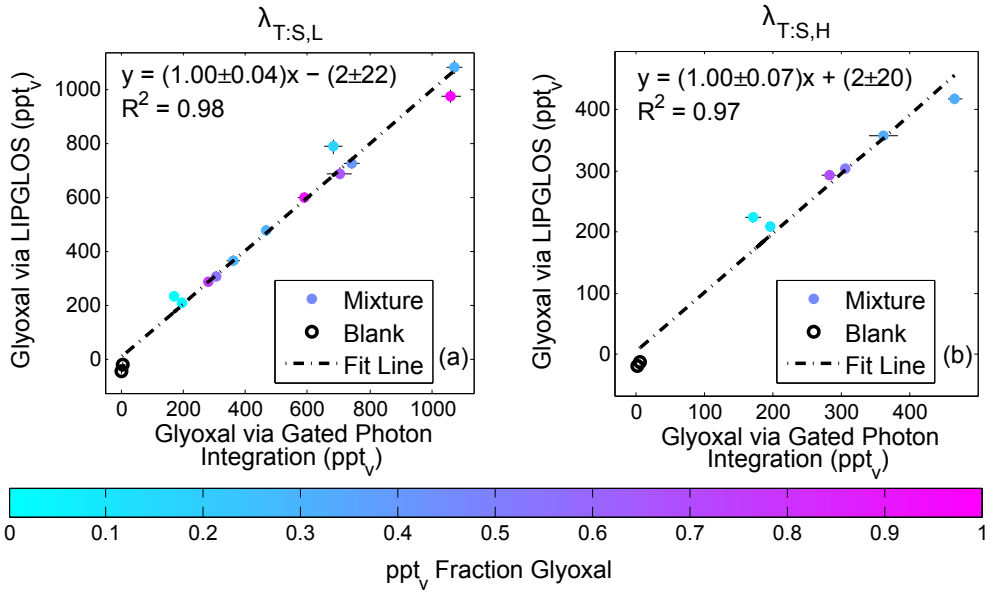

Fig. 6. Results from a simultaneous glyoxal calibration of the LIPGLOS and gated photon integration methods while varying methylglyoxal between 130–5400 pptv at $\lambda_{T:S,L}$ and 130–2500 pptv at $\lambda_{T:S,L}$ aside from the blanks. The color bar represents the fraction of total glyoxal and methylglyoxal pptv that is glyoxal. Displayed errors on y axis values are prefactor fit error. Error bars smaller than the plot markers are to be assumed smaller than the marker (± <19 pptv). **(a)** Mixing ratios determined by LIPGLOS method at $\lambda_{T:S,L}$ versus those determined by the gated photon integration method. **(b)** Analogous graph for $\lambda_{T:S,H}$.

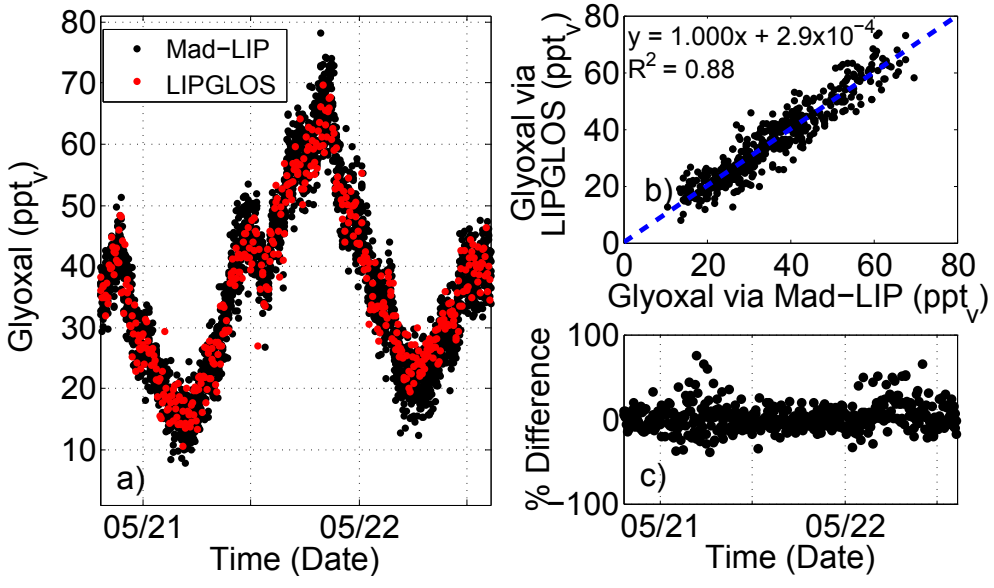

Fig. 7. **(a)** Glyoxal concentration time series from both Mad-LIP (40 s integration) and the LIPGLOS method (80 s integration). During early morning of the 21st when the concentrations are at their lowest, the standard deviation of the LIPGLOS and gated photon integration data is 4.0 pptv (extrapolated) and 2.9 pptv in 40 s, respectively. **(b)** Correlation of measurements coincident within 5 min. **(c)** Difference between the LIPGLOS method and Mad-LIP normalized to Mad-LIP measured glyoxal. During the day time hours, the standard deviation of the difference is 8 %. During the night, the deviation increases when the noise of the measurement allows values close to zero in the normalization value (glyoxal determined by Mad-LIP).

and 1.00 ± 0.07 at $\lambda_{T:S,L}$ and $\lambda_{T:S,H}$, respectively. The correlations do possess a non-zero y axis intercept value (-2 ± 22 at $\lambda_{T:S,L}$ and 2 ± 20 at $\lambda_{T:S,H}$), however they are statistically insignificant. While this analysis validates the presicion and robustness of the LIPGLOS method for glyoxal detection, one can also infer that the reliability of the methylglyoxal quantification (when methylglyoxal signal is comparable to that of glyoxal) is also high as it is determined in an identical manner.

4 Ambient observations

Ambient air was sampled during 20–22 May 2011 in downtown Madison, WI (Fig. 7). In the course of this period, the temperature ranged from 8 °C to 23 °C under partly cloudy skies. Data was collected using the tunable Ti:Sapphire laser to allow the best limits of detection presented in this work. Only the histograms taken at $\lambda_{T:S,H}$ were analyzed with the LIPGLOS method. The Mad-LIP instrument simultaneously collected data compatible with the LIPGLOS method as well as its native integration method for the purpose of comparison. During operation, the laser was dithered between $\lambda_{T:S,H}$ and $\lambda_{T:S,L}$; this dithering is required for the operation of the Mad-LIP instrument, however it reduces the duty cycle of collection of data appropriate for the LIPGLOS method. Values obtained via LIPGLOS were cross-calibrated with the gated photon integration method, which was calibrated in the fashion described elsewhere (Huisman et al., 2008). During the morning of the 21st when concentrations are the lowest, the standard deviation of the gated photon integration data is 2.9 pptv in 40 s and the LIPGLOS data is 2.5 pptv in 1.75 min (translating to 4.0 pptv in 40 sec). The precision error generated by LIPGLOS in the night time ambient data corresponds to a 5 min 3σ LoD of 4.4 pptv which is lower than what was calculated during the calibrations (11 pptv). Furthermore, this LIPGLOS LoD would be an upper limit as the precision error during that period incorporates some diurnal variation.

5 Conclusions

We have developed a method exploiting the difference in phosphorescent lifetimes of glyoxal and methylglyoxal to allow their simultaneous quantification in ambient air at a single wavelength. Speciation of composite signals is performed by fitting ambient phosphorescent decays to a linear combination of decays with known characteristic phosphorescent lifetimes established from laboratory experiments.

This method achieves atmospherically relevant 3σ limits of detection, the lowest of which were 4.4 pptv glyoxal in five minutes at $\lambda_{T:S,H}$ (440.136 nm, at the maximum of an absorption feature) during ambient measurements, and 243 pptv methylglyoxal in five minutes at $\lambda_{T:S,L}$ (440.104 nm) during calibration. Ambient data in Madison, WI showed that glyoxal concentrations as determined by the LIPGLOS method when compared to those achieved via the Mad-LIP instrument had a slope of 1.00 and a correlation coefficient of 0.88.

A major advantage of LIPGLOS over gated photon integration is that it does not require a tunable light source. This allows the use of simpler light sources, including high powered LEDs or laser diodes, which results in less expensive, lighter, more compact, more robust field instrumentation. Assuming a light source with 50 mW used for detection, a laser pulse width of 35 ns, and glyoxal and methylglyoxal cross sections at $\lambda_{T:S,H}$, the projected 5 min 3σ limits of detection are 2 pptv for glyoxal and 110 pptv for methylglyoxal. Alternatively, one can select a laser wavelength that, rather than optimized for glyoxal, is optimized to achieve similar sensitivities for both species. This would decrease the glyoxal interference in the methylglyoxal signal by choosing a wavelength of reduced glyoxal absorption, thereby decreasing the glyoxal sensitivity. Keeping previously assumed improvement parameters except using the wavelength 436.027 nm, where glyoxal and methylglyoxal cross-sections are 1.11×10^{-19} cm^2 molecule^{-1}, the projected 3σ limits of detection are 19 pptv for glyoxal and 99 pptv for methylglyoxal in 5 min.

This method permits instrumentation with ease of operation and components inexpensively purchased (~$40 k with the CrystaLaser and Alazar DAQ card, high powered LEDs could allow for ~$30 k with similar limits of detection), primarily due to the simple and inexpensive light source. Deployment of such instrumentation at established measurement sites would create a spatially detailed map of glyoxal and methylglyoxal, useful for either driving or as a comparison to regional-scale chemical models, as well as validation for satellite instruments. A candidate for such potential sites include the EPA atmospheric monitoring stations maintained all over the US that continuously measure particulate matter, NO_2, CO, and O_3, all of which are also tied to oxidative chemistry. The effect of transport between urban and rural areas on oxidation chemistry could be captured in this spatially detailed database of glyoxal and methylglyoxal concentrations.

Acknowledgements. The authors would like to thank Josh DiGangi for help with signal analysis and Andrew Huisman for preliminary studies. This work was funded by the L'Oréal USA Fellowships for Women in Science program as well as by the NSF, grant #0852406.

Edited by: D. Heard

References

Chan, A. W. H., Galloway, M. M., Kwan, A. J., Chhabra, P. S., Keutsch, F. N., Wennberg, P. O., Flagan, R. C., and Seinfeld, J. H.: Photooxidation of 2-Methyl-3-Buten-2-ol (MBO) as a Potential Source of Secondary Organic Aerosol, Envir. Sci. Tech., 43, 4647–4652, 2009.

Dubé, W. P., Brown, S. S., Osthoff, H. D., Nunley, M. R., Ciciora, S. J., Paris, M. W., McLaughlin, R. J., and Ravishankara, A. R.: Aircraft instrument for simultaneous, in situ measurement of NO_3 and N_2O_5 via pulsed cavity ring-down spectroscopy, Rev. Sci. Instrum., 77, 034101, doi:10.1063/1.2176058, 2006.

Fu, T.-M., Jacob, D. J., Wittrock, F., Burrows, J., Vrekoussis, M., and Henze, D.: Global budgets of atmospheric glyoxal and methylglyoxal, and implications for formation of secondary organic aerosols, J. Geophys. Res., 113, D15303, doi:10.1029/2007JD009505, 2008.

Galloway, M. M., Chhabra, P. S., Chan, A. W. H., Surratt, J. D., Flagan, R. C., Seinfeld, J. H., and Keutsch, F. N.: Glyoxal uptake on ammonium sulphate seed aerosol: reaction products and reversibility of uptake under dark and irradiated conditions, Atmos. Chem. Phys., 9, 3331–3345, doi:10.5194/acp-9-3331-2009, 2009.

Galloway, M. M., Huisman, A. J., Yee, L. D., Chan, A. W. H., Loza, C. L., Seinfeld, J. H., and Keutsch, F. N.: Yields of oxidized volatile organic compounds during the OH radical initiated oxidation of isoprene, methyl vinyl ketone, and methacrolein under high-NOx conditions, Atmos. Chem. Phys., 11, 10779–10790, doi:10.5194/acp-11-10779-2011, 2011.

Guenther, A., Hewitt, C., Erickson, D., Fall, R., Geron, C., Graedel, T., Harley, P., Klinger, L., Lerdau, M., Mckay, W., Pierce, T., Scholes, B., Steinbrecher, R., Tallamaraju, R., Taylor, J., and Zimmerman, P.: A global model of natural volatile organic-compound emissions, J. Geophys. Res.-Atmos., 100, 8873–8392, 1995.

Hallquist, M., Wenger, J. C., Baltensperger, U., Rudich, Y., Simpson, D., Claeys, M., Dommen, J., Donahue, N. M., George, C., Goldstein, A. H., Hamilton, J. F., Herrmann, H., Hoffmann, T., Iinuma, Y., Jang, M., Jenkin, M. E., Jimenez, J. L., Kiendler-Scharr, A., Maenhaut, W., McFiggans, G., Mentel, Th. F., Monod, A., Prévôt, A. S. H., Seinfeld, J. H., Surratt, J. D., Szmigielski, R., and Wildt, J.: The formation, properties and impact of secondary organic aerosol: current and emerging issues, Atmos. Chem. Phys., 9, 5155–5236, doi:10.5194/acp-9-5155-2009, 2009.

Ho, S. S. H. and Yu, J. Z.: Determination of airborne carbonyls: Comparison of a thermal desorption/GC method with the standard DNPH/HPLC method, Environ. Sci. Technol, 38, 862–870, 2004.

Horowitz, A., Meller, R., and Moortgat, G. K.: The UVVIS absorption cross sections of the -dicarbonyl compounds: pyruvic acid, biacetyl and glyoxal, J. Photoch. Photobio. A, 146, 19–27, 2001.

Huisman, A. J., Hottle, J. R., Coens, K. L., DiGangi, J. P., Galloway, M. M., Kammrath, A., and Keutsch, F. N.: Laser-induced phosphorescence for the in situ detection of glyoxal at part per trillion mixing ratios, Anal. Chem., 80, 5884–5891, 2008.

Isaksen, I. S. A., Granier, C., Myhre, G., Berntsen, T. K., Dalsøren, S. B., Gauss, M., Klimont, Z., Benestad, R., Bousquet, P., Collins, W., Cox, T., Eyring, V., Fowler, D., Fuzzi, S., Jöckel, P., Laj, P., Lohmann, U., Maione, M., Monks, P., Prevot, A. S. H., Raes, F., Richter, A., Rognerud, B., Schulz, M., Shindell, D., Stevenson, D. S., Storelvmo, T., Wang, W. C., van Weele, M., Wild, M., and Wuebbles, D.: Atmospheric composition change: Climate-Chemistry interactions, Atmos. Environ., 43, 5138–5192, 2009.

Kroll, J. H., Ng, N. L., Murphy, S. M., Varutbangkul, V., Flagan, R. C., and Seinfeld, J. H.: Chamber studies of secondary organic aerosol growth by reactive uptake of simple carbonyl compounds, J. Geophys. Res.-Atmos, 110, D23207, doi:10.1029/2005JD006004, 2005.

Lee, Y.-N., Zhou, X., and Hallock, K.: Atmospheric carbonyl compounds at a rural southeastern United States site, J. Geophys. Res., 100, 25933–25944, 1995.

Lippmann, M.: Health effects of tropospheric ozone, Environ. Sci. Technol., 25, 1954–1962, 1991.

Lohmann, U. and Feichter, J.: Global indirect aerosol effects: a review, Atmos. Chem. Phys., 5, 715–737, doi:10.5194/acp-5-715-2005, 2005.

Meller, R., Raber, W., Crowley, J. N., Jenkin, M. E., and Moortgat, G. K.: The UV-visible absorption spectrum of methylglyoxal, J. Photoch. Photobio. A, 62, 163–171, 1991.

Munger, J. W., Jacob, D. J., Daube, B. C., Horowitz, L. W., Keene, W. C., and Heikes, B. G.: Formaldehyde, glyoxal, and methylglyoxal in air and cloudwater at a rural mountain site in central Virginia, J. Geophys. Res., 100, 9325–9333, 1995.

O'Keefe, A. and Deacon, D. A. G.: Cavity Ring-down Optical Spectrometer for Absorption-Measurements Using Pulsed Laser Sources, Rev. Sci. Instrum., 59, 2544–2551, 1988.

Osthoff, H. D., Brown, S. S., Ryerson, T. B., Fortin, T. J., Lerner, B. M., Williams, E. J., Pettersson, A., Baynard, T., Dub, W. P., Ciciora, S. J., and Ravishankara, A. R.: Measurement of atmospheric NO_2 by pulsed cavity ring-down spectroscopy, J. Geophys. Res., 111, D12305, doi:10.1029/2005JD006942, 2006.

Paulot, F., Crounse, J. D., Kjaergaard, H. G., Kroll, J. H., Seinfeld, J. H., and Wennberg, P. O.: Isoprene photooxidation: new insights into the production of acids and organic nitrates, Atmos. Chem. Phys., 9, 1479–1501, doi:10.5194/acp-9-1479-2009, 2009.

Sinreich, R., Coburn, S., Dix, B., and Volkamer, R.: Ship-based detection of glyoxal over the remote tropical Pacific Ocean, Atmos. Chem. Phys., 10, 11359–11371, 2010, http://www.atmos-chem-phys.net/10/11359/2010/.

Spaulding, R. S., Schade, G. W., Goldstein, A. H., and Charles, M. J.: Characterization of secondary atmospheric photooxidation products: Evidence for biogenic and anthropogenic sources, J. Geophys. Res.-Atmos, 108, D4247, doi:10.1029/2002JD002478, 2003.

Stieb, D. M., Beveridge, R. C., Brook, J. R., Smith-Doiron, M., Burnett, R. T., Dales, R. E., Beaulieu, S., Judek, S., and Mamedov, A.: Air pollution, aeroallergens and cardiorespiratory emergency department visits in Saint John, Canada, J. Expo. Anal. Env. Epid., 10, 461–477, 2000.

Thalman, R. and Volkamer, R.: Inherent calibration of a blue LED-CE-DOAS instrument to measure iodine oxide, glyoxal, methyl glyoxal, nitrogen dioxide, water vapour and aerosol extinction in open cavity mode, Atmos. Meas. Tech., 3, 1797–1814, doi:10.5194/amt-3-1797-2010, 2010.

Tuazon, E. C., Atkinson, R., Mac Leod, H., Biermann, H. W., Winer, A. M., Carter, W. P. L., and Pitts, J. N.: Yields of glyoxal and methylglyoxal from the nitrogen oxide(NO_x)-air photooxidations of toluene and m- and p-xylene, Envir. Sci. Tech., 18, 981–984, 1984.

Turro, N. J. and Engel, R.: Quenching of Biacetyl Fluorescence and Phosphorescence, J. Am. Chem. Soc., 91, 7113–7121, 1969.

US EPA, Center for Environmental Research Information, Research and Development: Compendium of Methods for the Determination of Toxic Organic Compounds in Ambient Air, TO-11A, Center for Environmental Research Information, National Risk Management Laboratory, Office of Research and Development, US EPA, Cincinnati, OH, 2nd edn., 1999.

Volkamer, R., Molina, L. T., Molina, M. J., Shirley, T., and Brune, W. H.: DOAS measurement of glyoxal as an indicator for fast VOC chemistry in urban air, Geophys. Res. Lett., 32, L08806, doi:10.1029/2005GL022616, 2005a.

Volkamer, R., Platt, U., and Wirtz, K.: Primary and Secondary Glyoxal Formation from Aromatics: Experimental Evidence for the BicycloalkylRadical Pathway from Benzene, Toluene, and p-Xylene, J. Phys. Chem. A, 105, 7865–7874, 2005b.

Volkamer, R., Spietz, P., Burrows, J., and Platt, U.: High-resolution absorption cross-section of glyoxal in the UV-vis and IR spectral ranges, J. Photoch. Photobio. A, 172, 35–46, 2005c.

Volkamer, R., San Martinti, F., Molina, L. T., Salcedo, D., Jimenez, J., and Molina, M. J.: A missing sink for gas-phase glyoxal in Mexico City: Formation of secondary organic aerosol, Geophys. Res. Lett., 34, L19807, doi:10.1029/2007GL030752, 2007.

Vrekoussis, M., Wittrock, F., Richter, A., and Burrows, J. P.: Temporal and spatial variability of glyoxal as observed from space, Atmos. Chem. Phys., 9, 4485–4504, 2009, http://www.atmos-chem-phys.net/9/4485/2009/.

Vrekoussis, M., Wittrock, F., Richter, A., and Burrows, J. P.: GOME-2 observations of oxygenated VOCs: what can we learn from the ratio glyoxal to formaldehyde on a global scale?, Atmos. Chem. Phys., 10, 10145–10160, doi:10.5194/acp-10-10145-2010, 2010.

Washenfelder, R. A., Langford, A. O., Fuchs, H., and Brown, S. S.: Measurement of glyoxal using an incoherent broadband cavity enhanced absorption spectrometer, Atmos. Chem. Phys., 8, 7779–7793, doi:10.5194/acp-8-7779-2008, 2008.

Wittrock, F., Richter, A., Oetjen, H., Burrows, J., Kanakidou, M., Myriokefalitakis, S., Volkamer, R., Beirle, S., Platt, U., and Wagner, T.: Simultaneous global observations of glyoxal and formaldehyde from space, Geophys. Res. Lett., 33, L16804, doi:10.1029/2006GL026310, 2006.

Yu, G., Bayer, A. R., Galloway, M. M., Korshavn, K. J., Fry, C. G., and Keutsch, F. N.: Glyoxal in Aqueous Ammonium Sulfate Solutions: Products, Kinetics and Hydration Effects, Environ. Sci. Technol., 45, 6336–6342, doi:10.1021/es200989n, 2011.

Zalicki, P. and Zare, R. N.: Cavity ring-down spectroscopy for quantitative absorption measurements, J. Chem. Phys., 102, 2708–2717, 1994.